Proceedings of ASME Turbo Expo 2012: Power for Land, Sea and Air
GT2012
June 11-15, 2012, Copenhagen, Denmark

GT2012-69114

PREDICTIONS OF ROTORDYNAMIC PERFORMANCE FOR ELECTRIC TURBOCOMPOUND

Keun Ryu
Senior Development Engineer
kryu@borgwarner.com

Augustine Cavagnaro
Product Manager
acavagnaro@borgwarner.com

Global Commercial Diesel Product Development
BorgWarner Turbo Systems
Arden, NC 28704

ABSTRACT

An electric turbocompound (ETC) system for heavy duty diesel engines offers significant system level benefits, such as improved fuel efficiency and reduced NO_x emissions with a lower CO_2 footprint. Presently, a high speed switched reluctance type motor/generator is integrated into a turbocharger shaft between the turbine and compressor wheels. The motor assists rapid acceleration of the turbocharger shaft, thereby rendering faster transient response. At steady or over-boost operating conditions, the generator provides electric power which can be used directly or stored in an on-board storage device. ETCs operate at high rotational speeds and, if equipped with fluid film bearings, use pressurized engine oil to lubricate the bearings (journal and thrust). This paper presents comprehensive predictions of the linear and nonlinear shaft motions of an ETC supported on floating ring bearings. A rotor structural finite element model integrates the floating ring bearing model for prediction of the rotor-bearing system (RBS) linear and nonlinear forced responses under actual operating conditions. Predictions show a complex rotordynamic behavior of the RBS with large amplitude subsynchronous motions over a wide speed range. However, the subsynchronous whirl motions reach a limit cycle enabling continuous operation without system failure. Most importantly, stiffness of the lamination stack mounted on the shaft has a significant effect on the amplitude and frequency content of the shaft motion. The present analysis effectively aids to accelerate ETC prototype development with increased reliability and product troubleshooting.

1. INTRODUCTION

Turbochargers increase the mass of air forced into the cylinders of internal combustion engines (ICEs) by increasing air density, thereby increasing the power output of the engine. This enables smaller and more fuel-efficient ICEs [1]. Figure 1 depicts a schematic view (not to scale) of a turbocharger supported on floating ring bearings (FRBs). The major components of the turbocharger are the turbine, compressor, shaft, bearings, and housings. Oil is supplied through the bearing housing and flows into two FRBs. Each bearing has two fluid films in series; inner and outer films separate the shaft OD from the ring ID and the ring OD from the bearing housing ID, respectively. Exhaust gases drive a turbine which is connected to a compressor through a thin solid shaft. Then, the compressor forces compressed air into the engine cylinder, thereby improving combustion efficiency and power output.

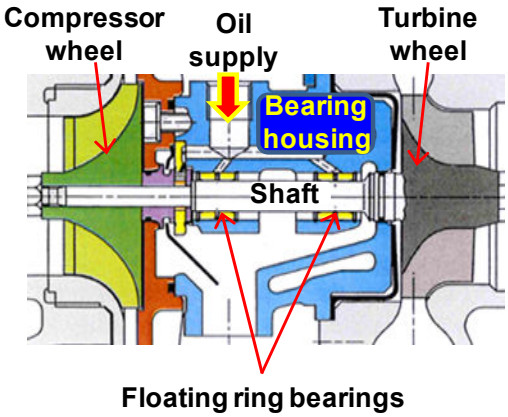

Fig. 1 Schematic view (not to scale) of typical commercial turbocharger rotor-bearing system. Reproduced from [2]

An electric turbocompound (ETC) system promises a significant improvement in boost pressure during transient events, thereby providing an effective solution to turbo-lag [3-5]. Furthermore, an ETC generates electric power for a vehicle's auxiliary systems [6]. Smaller engines, enabled by an integrated electric machine with enhanced transient response, also aid to satisfy environmental restrictions by reducing fuel consumption and CO_2 output.

Presently, an ETC integrates a switched reluctance (SR) motor/generator into a turbocharger shaft between the turbine and compressor wheels. SR machines enable simple and rugged

structure. SR machines consist of a stator with excitation windings and magnetic rotor with saliency. The most notable feature of SR machines is no windings or permanent magnets on the rotors; therefore, the only excitation source consists of stator windings. Hence, the resistive winding losses in SRMs occur on the stator. This enables easy and effective cooling strategy for SR machines [7]. References [8-12] report the recent efforts to demonstrate high speed turbomachinery at extreme temperatures deploying SR machines. Note that careful thermal and mechanical stress managements are mandatory when incorporating a SR motor/generator into a high temperature application.

The rotor-bearing system is one of the most important design features for a reliable turbocharger since the static and dynamic forced performance of the turbocharger significantly relies on its bearing system. Most commercial automotive turbochargers integrate engine oil lubricated FRBs (or semi-FRBs[1]) because of their low cost and reduced power losses [13]. Figure 2 illustrates a schematic view for a typical FRB. FRBs are prone to show (one or multiple) subsynchronous motions of large amplitude, caused by the circumferential flow (shearing) within inner and outer films, over extended operating speed ranges [14]. Nonetheless, FRBs reach stable limit cycles enabling continuous operation, thereby providing a cost-effective solution for automotive turbochargers. References [15-20] provide extensive review of relevant literature on FRBs (as well as semi-FRBs) and present comprehensive comparison of predictions to measured shaft motions and TC casing accelerations.

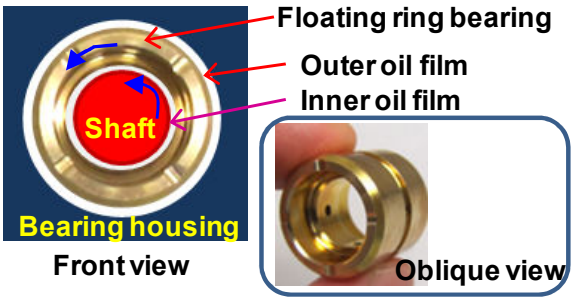

Fig. 2 Photograph of a floating ring bearing for automotive applications. Shaft and oil films not to scale.

This paper presents the linear and nonlinear rotordynamic analyses of a rotor-bearing system for an ETC. The linear rotordynamic model with linearized bearing force coefficients predicts the rotor free-free modes, the onset speed of instability, and the synchronous response to imbalance. The nonlinear response model predicts amplitudes and whirl frequencies of sub harmonic motions, as well as the overall shaft motions. The current study also quantifies the effect of stiffness of the lamination stack of the shaft on rotordynamic forced performance. The present analysis will aid in reducing overall product development time and expenditures. Note that turbocharger performance qualification typically requires extensive testing that is expensive and time-consuming.

[1] In a semi-floating ring bearing (SFRB), the floating ring is locked by a pin which prevents the rotation of the ring, i.e., the outer oil film acts as a squeeze film damper (SFD).

2. ETC STRUCTURAL AND FLOATING RING BEARING MODELS

Figure 3 shows the ETC rotor structural model consisting of 55 finite elements for the rotor, including the thrust collar, washer, and nut. The compressor and turbine wheels (the circles in the figure) are modeled as added lumped mass and mass moments of inertia (transverse and polar), as is common in rotor modeling [21]. Table 1 lists the mass and inertias of the compressor and turbine wheels. The thrust collar, thrust washer, nut, compressor-end and turbine-end collars are considered to contribute fully to the bending stiffness of the shaft. In the figure, springs connecting the bearings to ground represent the outer fluid films. The inner film connections are not visible. The model includes imbalance mass distributions in 4 planes (the triangles in the figure); nose and back planes of the compressor wheel (CW), and back and front faces of the turbine wheel (TW). In the present analysis, the imbalance masses are ~0.36 g-mm at compressor nose and back surface, and ~0.22 g-mm at turbine nose and back surface, with ~60° phase difference between CW and TW.

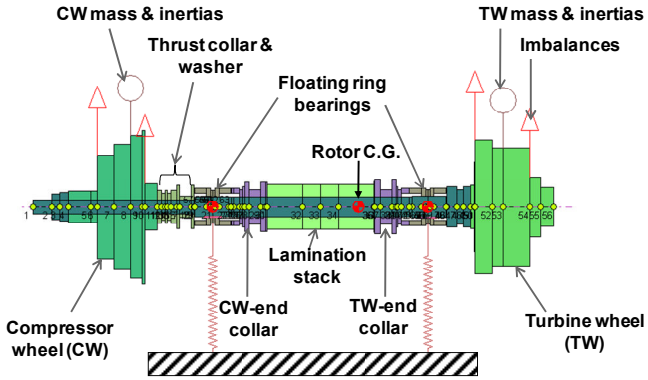

Fig. 3 ETC structural finite element model of rotor and floating ring bearings

Table 1. Mass and inertias of compressor and turbine wheels

Component	Mass [kg]	Transverse moment of inertia [kg-m^2]	Polar moment of inertia [kg-m^2]
Compressor wheel	0.072	1.69×10^{-5}	2.32×10^{-5}
Turbine wheel	0.231	4.33×10^{-5}	4.56×10^{-5}

The present system integrates a three-phase SR machine with 6 stator poles and 4 rotor poles (i.e., 6/4 topology). The configuration does not have any zero-torque position[2] and enables a constant torque output independent of rotor position. The CW and TW are taken from a commercial turbocharger (namely, a baseline turbocharger) and the shaft and bearings are modified to employ a lamination stack at the rotor mid-span. The lamination stack is modeled as 4 finite elements as shown in Fig. 3[3]. Note that the *effective* material properties of the

[2] For a symmetric SRM with m stator poles and n rotor poles, zero torque positions exist if the ratio m/n is an integer [7].

[3] Presently, the rotor is modeled using axisymmertic beams in a 2-dimensional system. This limits the modeling of "real" structures of the rotating components. Unfortunately, a beam element cannot represent an entire "actual" system.

lamination largely determine the overall rotor structural characteristics. It is incorrect to model the stiffness of the rotor without the lamination stack [21,22]. Incidentally, large clamping pressure (i.e., axial compressive force) to the lamination stack could increase its stiffness contribution to the shaft. References [21,23] show the effective modulus of the stack increases linearly with compressive stress.

Since the actual stiffness of the lamination stack is currently unknown without actual hardware, extensive rotordynamic analyses are conducted for two cases: no stiffness from the stack (i.e., the lamination stack is of null modulus value with actual density) and full stiffness from the stack (i.e., the lamination stack has an actual material modulus value and density). To accurately determine the contribution of the lamination stack to the ETC's shaft stiffness, a series of impact tests for the rotor are necessary (when the test components are available)[4]. Note that validation of the ETC rotordynamic model requires good correlation between measured and predicted rotor physical properties, as well as free-free natural frequencies and mode shapes. This is mandatory for providing the accuracy of the rotor structural model.

FRBs have two fluid films in series. The inner and outer film clearances along with the lubricant viscosity within each film mainly determine the FRB forced performance. Viscous shear in the inner film renders the rotation of the floating ring, while shear in the outer film retards its motion. The ring spins at a fraction of rotor speed, thereby reducing the shear drag losses [15]. The rotational speed of the ring determines the steady state and dynamic forced response of a rotor-bearing system. In operation, the mechanical energy is carried away (convected) by the lubricant and conducted through the ring and bearing. Temperature rise in the bearings reduces the lubricant viscosity and changes bearing operating clearances due to thermal expansion of the components. The balance of drag torques acting on the ring inner and outer surfaces determines the ring rotational speed [15]. Each FRB supports a static load equal to a fraction of the rotor weight[5].

The FRB model, based on the numerical solution of the laminar flow Reynolds equation on the inner and outer fluid films and integrated into a commercial nonlinear rotordynamics computational tool [24], predicts the static load parameters and the rotordynamic force coefficients of the inner and outer films as a function of the load applied at a given rotor speed. Note that the operating clearance, the effective lubricant viscosity, and the actual load conditions (static and dynamic), are the most important parameters for accurate estimation of an ETC dynamic forced response. The current prediction accounts for the decrease in oil viscosity due to high temperature operation (lubricant: SAE 10W30) and the net thermal expansion of the shaft, bearing housing, and floating rings that significantly change the bearing operating clearances. The turbine and compressor bearing temperatures are estimated from proprietary baseline turbocharger experimental data (turbine side bearing: 150°C and compressor side bearing: 125°C). At a hot operating condition (i.e., an industrial standard gas stand test), the turbine-end bearing inner clearance increases by ~44% and its outer clearance decreases by ~19% while the compressor-end bearing inner clearance increases by ~33% and its outer clearance decreases by ~17%. Centrifugal growths of the rotating shaft and ring, a function of their geometry and material properties [25], are just ~0.25 μm and ~0.05 μm, respectively; therefore, this effect is not accounted for in the model.

Table 2 lists the material properties of the rotating components and the bearing housing at room temperature. Note that in real operation at high temperature, the materials are not impervious to heat and suffer material softening as their temperature increases.

Table 2 Material properties of rotor components and bearing housing

Component	Material	Density [kg/m^3]	Elastic modulus [GPa]	Shear modulus [GPa]	Poisson's ratio	Thermal expansion coefficient [10^{-6}/K]
Shaft, thrust collar , thrust washer, and nut	AISI 4140	7860	204	79	0.3	12
Compressor wheel	Aluminum alloy	2750	70	26	0.22	5.5
Turbine wheel	Inconel 718	7910	202	80	0.28	13
Floating ring bearing	Special brass	8100	105	39	0.35	20.4
Bearing housing	Cast iron	7150	240	67.6	0.37	12.5

The equations of motion for the ETC rotor-bearing system are [26]

$$M\ddot{u} + C\dot{u} + \Omega G\dot{u} + Ku = F \quad (1)$$

where M, C, and K are inertia, damping and stiffness matrices and G is the gyroscopic moments matrix. u is the rotor and floating ring response vector. F is a vector of external and bearing reaction forces and moments, and consists of a vector of static loads (F_S), a vector of force from imbalance masses (F_{Imb}), a vector of force from the fluid film bearing reaction forces (F_{FRB}), and a vector of external excitation forces and moments (F_{Ext}), i.e., $F=F_S+F_{Imb}+F_{FRB}+F_{Ext}$. Note that F_{FRB} has a cross-coupled term and relies on the rotor instantaneous position (u) and velocity ($\dot{u}$). Therefore, for the nonlinear rotordynamic analysis, F_{FRB} is calculated at each time step and integrated into the system equations of motion. Each node for the rotor structural finite element has four degrees of freedom; two lateral and two rotational displacements. Note that all rotor dynamic motion amplitudes are referenced to a fixed coordinate system (i.e., absolute values). Presently, it is assumed that the ETC housing is not subjected to any external loading.

[4] The *simple* rap test consists of suspending the rotor, impacting the rotor with a hammer, and recording the amplitude of the transfer function between a stationary and a roaming accelerometer versus the rotor axial length.

[5] Actual static load acting on a bearing is unknown since the compressor and turbine also impose side aerodynamic loads, with magnitudes increasing rapidly as the shaft speed rises. The present bearing computational model does not consider the effect of feed oil pressure into the bearings. San Andrés *et al.* [17] show that feed oil pressure exerts a significant side load on small turbochargers.

3. PREDICTIONS OF ETA ROTOR-BEARING SYSTEM RESPONSE

3.1 Full Stiffness Contribution of Lamination Stack to Rotor Mid-Span

3.1.1 Linear analysis.

To add significant stiffening effect to the rotor mid-span, the material properties of the lamination stack calculated from the rule of the mixtures[6] [27] are used in the rotor structural model (namely, *full stiffness* lamination stack). In practice, an appropriately reduced lamination material modulus can be used as an input of the rotor model when some stiffness contribution is present.

Figure 4 depicts the predicted free-free mode shapes corresponding to the first and second natural frequencies for the *full stiffness* lamination stack. The first and second elastic (i.e., bending) modes are ~60 krpm and ~160 krpm, respectively. Note that the ETC traverses the system bending critical speed since its maximum operating speed is ~150 krpm.

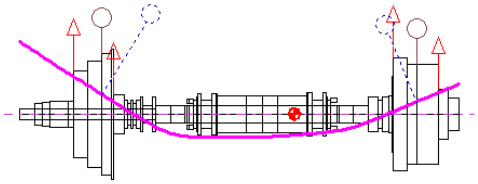

(a) 1st free-free natural frequency (~60 krpm) and mode shape

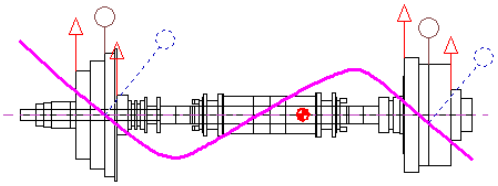

(b) 2nd free-free natural frequency (~160 krpm) and mode shape

Fig. 4 Full stiffness contribution of lamination stack to the rotor mid-span: Predicted 1st and 2nd free-free natural frequencies and mode shapes of ETC rotor.

The linear eigenvalue analysis predicting the rotor-bearing system natural frequencies and damping ratios incorporates the linearized force coefficients (stiffness and damping) for the inner and outer films of the bearings. Figures 5 and 6 depict the dimensionless force coefficients (defined in [28][7]) of FRB inner and outer films calculated at a whirl frequency synchronous with rotor speed for the compressor-end and turbine-end bearings, respectively[8]. The inset in the figure shows a schematic view of the coordinate system. As the rotor speed increases, the fluid film direct stiffnesses are nearly zero because of the very low static loads on the bearings. Note that the cross-coupled stiffnesses are higher than the direct stiffness. On the other hand, the direct damping coefficients are higher than the cross-coupled damping coefficients. The damping coefficients decrease with rotor speed since the rotor and floating ring move towards the bearing center as the rotor speed increases. It is important to note that (K_{xy}>0 and K_{yx}<0) provides energy to forward whirl and K_{xy} =-K_{yx} renders a tangential (or normal to radial) force normal to the rotor whirl orbit (i.e., a typical drive of rotor-bearing system instability) [29].

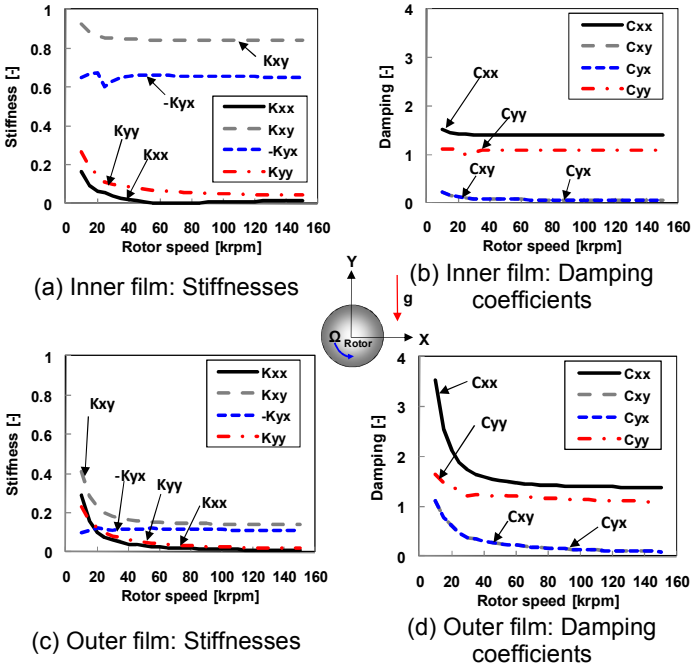

(a) Inner film: Stiffnesses (b) Inner film: Damping coefficients

(c) Outer film: Stiffnesses (d) Outer film: Damping coefficients

Fig. 5 Compressor-end bearing: Predicted FRB normalized direct and cross-coupled force coefficients versus rotor speed. Whirl frequency equals rotor speed.

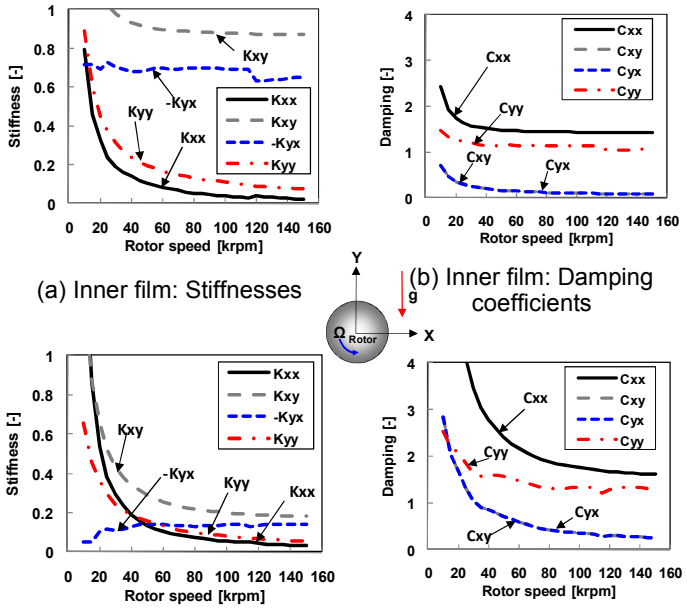

(a) Inner film: Stiffnesses (b) Inner film: Damping coefficients

(c) Outer film: Stiffnesses (d) Outer film: Damping coefficients

Fig. 6 Turbine-end bearing: Predicted FRB normalized direct and cross-coupled force coefficients versus rotor speed. Whirl frequency equals rotor speed.

---

[6] This method takes the full modulus of elasticity of the lamination (210 GPa) and glue (3 GPa) materials.

[7] $\bar{k} = K_B / [\mu \frac{D}{2} (\frac{L}{c_r})^3 \Omega]$ and $\bar{c} = C_B / [\mu \frac{D}{2} (\frac{L}{c_r})^3]$ where K_B and C_B are the calculated forced coefficients (stiffness and damping), μ is the lubricant viscosity, Ω is the rotor/ring speed, D is the (cold) rotor/ring diameter, L is the (cold) bearing film length, and c_r is the (cold) bearing radial clearance.

[8] Complete information on the FRB geometry is proprietary; hence, it is not listed in this paper. The authors apologize in advance for this limitation.

Figures 7 and 8 depict the predicted damped natural frequency map and damping ratios of the ETC rotor-bearing system, respectively, along with corresponding forward precessional rotor natural mode shapes: two rigid conical and cylindrical modes, two modes with bearing ringing modes, and two elastic modes. The black dashed line denotes the rotor synchronous speed (1X=Ω), 50% of rotor speed (0.5Ω), ring rotational speed (~0.22Ω)[9], and 50% of ring rotational speed (~0.11Ω). Only the first elastic mode shape corresponds with a rotor speed at ~60 krpm. The 1st and 2nd rigid mode natural frequencies range from ~30 Hz to ~150 Hz as rotor speed increases. These modes are well-damped below ~40 krpm; however, they are unstable at rotor speed above ~50 krpm (i.e., negative damping ratios). The 4th natural frequency corresponds to a conical mode with the floating ring whirling in a cylindrical mode. This mode is also unstable at rotor speed below ~100 krpm and above ~125 krpm. Note that the linear rotordynamic analysis is representative only of small amplitude motions about the (static) equilibrium condition.

Figure 9 depicts the predicted amplitude of imbalance synchronous rotor response at the compressor end obtained from the linear analysis. The amplitudes of response are normalized with respect to the maximum physical displacement at the compressor end. The synchronous response from the linear rotordynamic analysis shows peak amplitude at ~60 krpm. As shown in Fig. 7, the 1st elastic mode (ζ=0.03) coincides with the rotor synchronous speed (Ω) at this frequency.

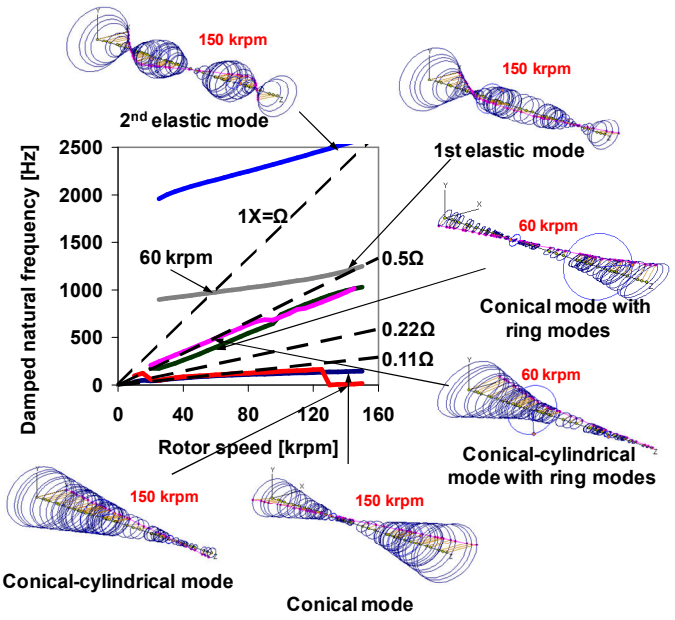

Fig. 7 Full stiffness contribution of lamination stack to the rotor mid-span. Linear analysis: Predicted damped natural frequency map of ETC rotor-bearing system. Forward modes shown.

[9] The ring speed ratios (=ring speed/rotor speed) for the compressor-end and turbine-end bearings are 0.20 and 0.22, respectively.

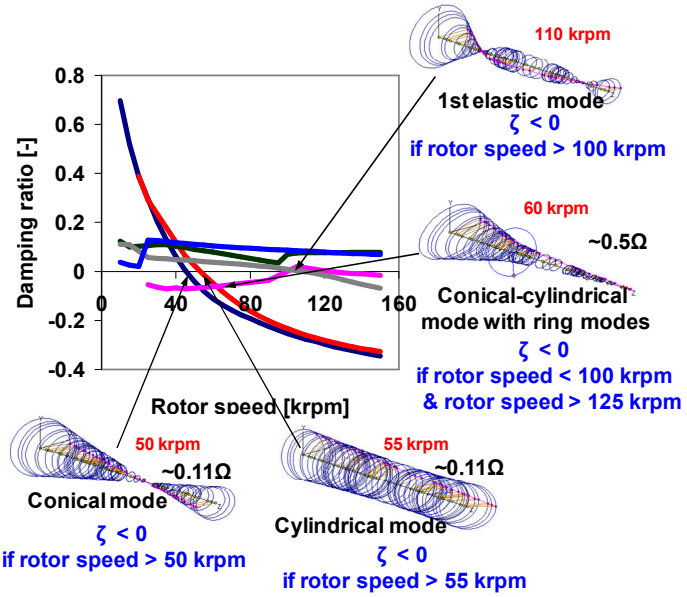

Fig. 8 Full stiffness contribution of lamination stack to the rotor mid-span. Linear analysis: Predicted ETC rotor-bearing system damping ratios versus rotor speed. Forward (unstable) modes shown.

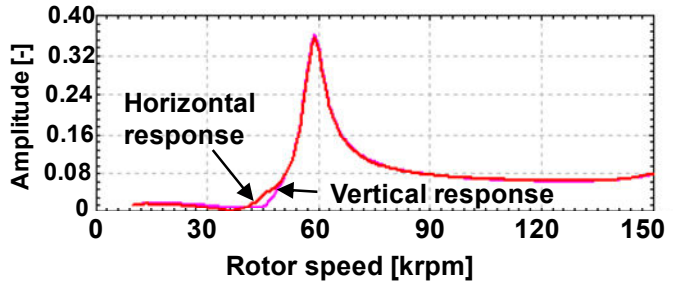

Fig. 9 Shaft motions at compressor end. Full stiffness contribution of lamination stack to the rotor mid-span. Linear analysis: Lag phase angle and amplitude and of synchronous response.

3.1.2 Nonlinear analysis.

For the nonlinear rotordynamic analysis, the instantaneous reaction force of the fluid film bearings are applied into the ETC rotor-bearing system equations of motion. For numerical integration, Wilson-theta method is used in all calculations with a time step increment of 1.5×10^{-6} s and time duration 0.09 s for each rotor speed [24]. The total number of integration points (samples) is 32,609 for each rotor speed. The rotor speed increases from 10 krpm to 150 krpm. Note that in the analysis, the rotor speed is held constant. Thus, the prediction represents (quasi) steady-state conditions at a particular rotor speed. At each rotor speed, the numerical integration of the system equations of motion proceeds for many shaft revolutions until a steady limit cycle is reached. FFTs of the rotor-FRB time response are obtained in the post-processing and the waterfall graph is assembled.

Note that a nonlinear analysis determines the threshold of instability as a bifurcation from a single point into a limit cycle of a single frequency or a quasi-periodic orbit [30]. Internal and combined resonances are not uncommon in nonlinear multiple degree of freedom mechanical systems [31].

Figure 10 depicts the predicted waterfall plots (amplitude and frequency content, and contour plots) of vertical (i.e., gravity plane) rotor motions at the compressor end. The synchronous response is labeled as Ω(=shaft rotational speed). From 10 krpm to 60 krpm, there is dominance of synchronous rotor motions. On the other hand, above ~65 krpm, rotor synchronous motion amplitudes, i.e., response to imbalance, are a minute fraction of the shaft total motion. The first subsynchronous whirl frequencies from 65 krpm to the top rotor speed are at ~50% of floating ring rotational speed (i.e., ~0.11Ω) denoting a characteristic instability of the outer fluid film. The first whirl frequency increase linearly with rotor speed and follows the conical (or conical-cylindrical) mode up to the top speed, recall Fig. 7. The second subsynchronous motions of lesser amplitude at rotor speed > ~130 krpm appear at ~50 % of rotor speed (i.e., ~0.5Ω). This subsynchronous frequency is characteristic of the inner film instability.

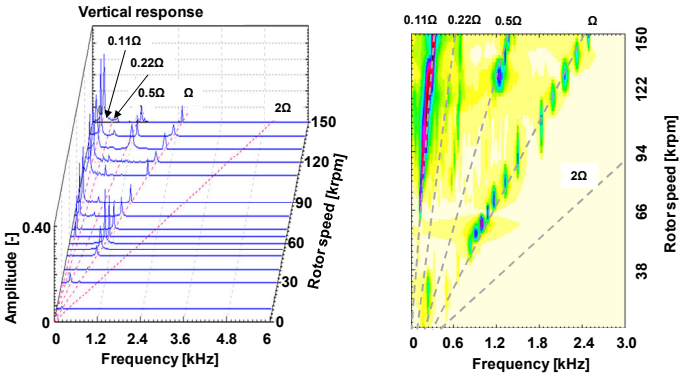

Fig. 10 Full stiffness contribution of lamination stack to the rotor mid-span. Nonlinear analysis: Waterfalls of predicted ETA shaft motions at compressor end.

Note that the rotor forced modes corresponding to the first and second whirl frequencies above ~65 krpm resemble those obtained from the system linear eigenvalue analysis (see Fig. 7). However, since the linear rotordynamic analysis is valid only for small amplitude motions about the equilibrium condition, the whirl frequencies from the nonlinear forced response model are not identical with the predicted (linear) system natural frequencies. In addition, there is little discrepancy between the linear RBS response (Fig. 9) and the synchronous response obtained from nonlinear analysis (Fig. 10). However, recall the abundant sub harmonic motions found and displayed in Fig. 10. It is important to note that linear rotordynamic analysis produces satisfactory predictions for speed ranges up to the onset of instability [16,32]. Instabilities associated to the loss of damping are found at a certain threshold rotor speed, recall Fig. 8.

Predicted motions along the horizontal direction are not shown for brevity. The horizontal displacements are also rich in subsynchronous components as in the vertical motions.

Accurate prediction of overall shaft motion (i.e., peak-to-peak amplitude of the complex orbital shape) is of the utmost importance to the turbocharger manufacturer for qualification of its product. At rotor speeds of 50, 70, 90, and 150 krpm, Fig. 11 depicts transient motions of the ETC rotor and rotor whirl orbits (unfiltered) at the compressor-end and turbine-end bearings. The inset figure shows the rotor structural model and the location of the FRBs. Note that all rotor whirl orbit amplitudes are made dimensionless relative to the maximum physical displacement at each bearing location. The ETC shaft motions reach limit cycles within the rotor-bearing clearance physical limit (between 10~70% of the maximum allowed shaft motions), which allows the ETC to operate safely at high speeds. Note that the nonlinear behavior, i.e., low frequency (mainly conical mode) limit cycles of large amplitude, is typical of turbochargers supported on (lightly loaded) floating ring bearing systems.

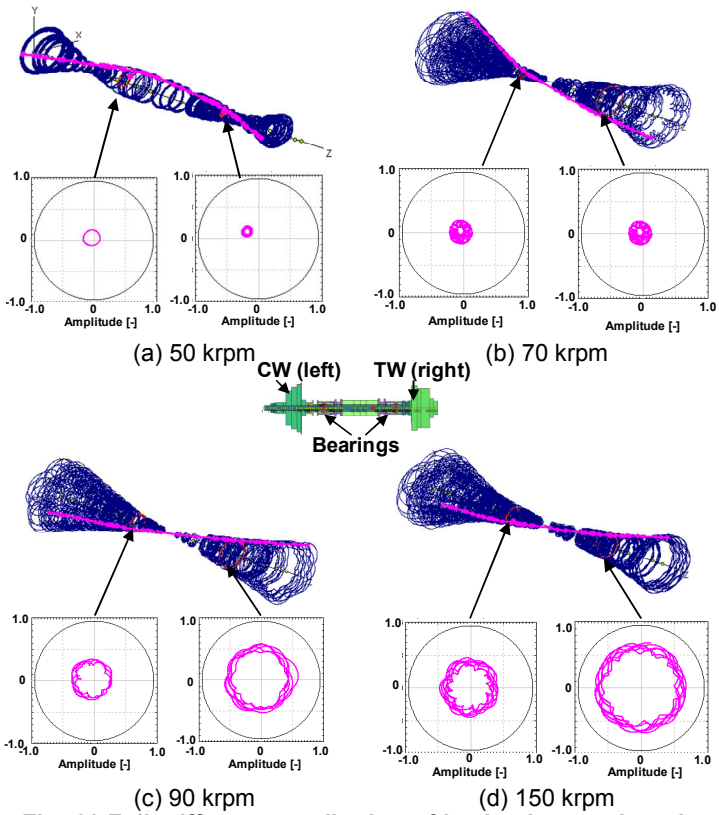

Fig. 11 Full stiffness contribution of lamination stack to the rotor mid-span. Nonlinear analysis: Rotor transient motions and whirl orbits (unfiltered) at bearing locations. Rotor speed of 50, 70, 90, and 150 krpm

3.2 No Stiffness Contribution of Lamination Stack to Rotor Mid-Span

Presently, *no stiffness* lamination stack represents no additional stiffness contribution from the lamination stack to the shaft. That is, the density of the lamination stack is retained but the modulus is set to zero. Therefore, the lamination stack is not included in the bending stiffness model of the rotor.

Figure 12 shows the predicted free-free mode shapes corresponding to the first and second natural frequencies for the *no stiffness* lamination stack. The first and second elastic (i.e., bending) modes are ~32 krpm and ~131 krpm, respectively. Note that, for rotor operation up to 150 krpm, the ETC with the *no stiffness* lamination stack crosses the first and second system bending critical speeds. Recall that the ETC shaft with the *full stiffness* lamination stack shown in Fig. 4 renders the first and second free-free natural frequencies at ~60 krpm (~88% higher than Fig. 12 (a)) and ~160 krpm (~22% higher than Fig. 12(b)),

respectively. Details on linear eigenvalue analysis are omitted for brevity.

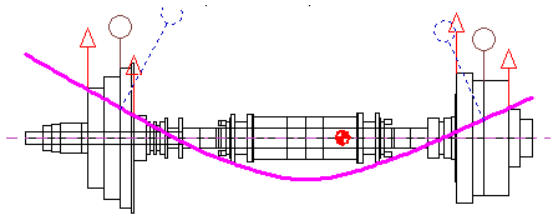

(a) 1st free-free natural frequency (~32 krpm) and mode shape

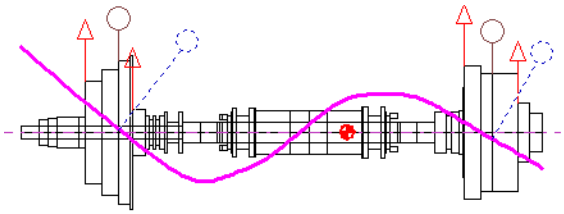

(b) 2nd free-free natural frequency (~131 krpm) and mode shape

Fig. 12 No stiffness contribution of lamination stack to the rotor mid-span: Predicted 1st and 2nd free-free natural frequencies and mode shapes of ETC rotor.

Figure 13 depicts the predicted waterfall of ETC shaft motion at the compressor end along the vertical direction (i.e., gravity plane). The figure also shows the contour map of shaft motions. The prediction shows two notable subsynchronous whirl motions at ~50% ring speed above 50 krpm and ~50% shaft speed below 70 krpm. In particular, beyond 70 krpm, the response amplitudes due to rotor imbalance are just a small fraction (10~20% or less) of the total amplitude of motion.

To quantify the stiffness effect of the lamination stack on the onset and persistence of sub harmonic whirl motions, compare the present waterfall plot with that for the *full stiffness* lamination stack, see Fig. 11. The lamination stack stiffness remarkably changes the onset and amplitude severity of subsynchronous whirl motions. The stiff rotor due to *full stiffness* lamination stack exacerbates the severity of the subsynchronous response. Note that at the ~50% frequency whirl (~0.5Ω) disappears for rotor speed > ~90 krpm.

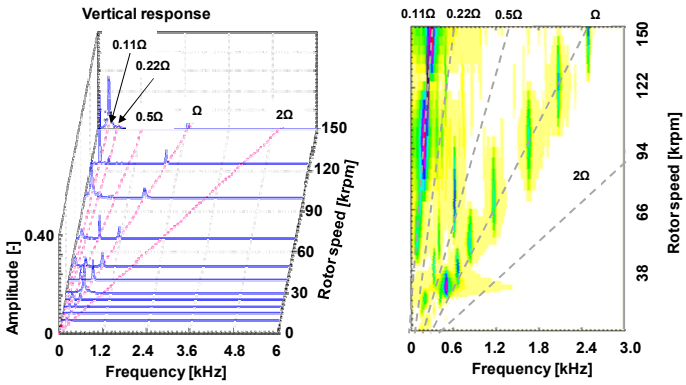

Fig. 13 No stiffness contribution of lamination stack to the rotor mid-span. Nonlinear analysis: Waterfalls of predicted ETA shaft motions at compressor end.

At rotor speeds of 30, 50, 90, and 150 krpm, Fig. 14 depicts transient motions of the ETC rotor and rotor whirl orbits (unfiltered) at the compressor-end and turbine-end bearings. The inset figure shows the rotor structural model and the location of the FRBs. Rotor whirl orbit amplitudes are made dimensionless relative to the physical limit at each bearing location. The overall amplitudes of shaft motion at the bearing locations, increasing with rotor speed, are <70% of the physical limit, i.e., within well-confined physical limits.

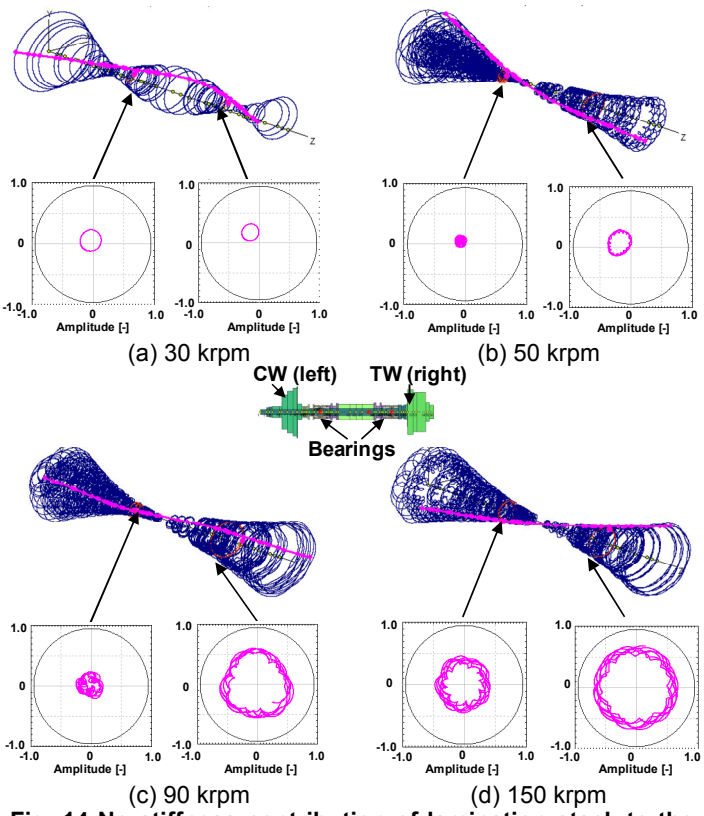

Fig. 14 No stiffness contribution of lamination stack to the rotor mid-span. Nonlinear analysis: Rotor transient motions whirl orbits (unfiltered) at bearing locations. Rotor speed of 30, 50, 90, and 150 krpm

4 CONCLUSIONS AND FUTURE WORK

The paper presents the linear and nonlinear rotordynamic models of the rotor-bearing system for an ETC. The shaft of the ETC is supported on FRBs. Changes in operating clearance due to thermal expansion of the system components and effective lubricant viscosity are most important for accurate prediction of ETC dynamic forced response. Linear rotordynamic analyses predict natural frequencies and damping ratio of the rotor-bearing system from an eigenvalue analysis. The nonlinear rotordynamic model integrates the rotor equations of motion with each bearing for prediction of system time responses. The fluid film reaction forces depend on the instantaneous shaft and ring displacements and velocities, bearing geometry, and operating conditions. Nonlinear predictions show two distinctive subsynchronous motions of significant amplitudes (limit cycles) over a wide speed range. Stiffness of the lamination stack mounted on the shaft clearly shows a pronounced effect on the amplitude and frequency content of the ETC shaft motion. If the lamination stack adds significant

stiffness to the rotor mid-span (i.e., *full stiffness* lamination stack), whirl motions at ~50% shaft speed appear at 130 krpm and endure to the highest shaft speed (150 krpm). In addition, larger stiffness of the lamination stack produces higher amplitudes of the first subsynchronous whirl (~50% ring speed) motion at the bearings. The motions with the whirl frequency at ~50% ring speed persist from 65 krpm and 50 krpm to the top speed for *full stiffness* and *no stiffness* lamination stacks, respectively. For both cases, the largest subsynchronous amplitudes concentrate at whirl frequencies ~50% of floating ring rotational speed, thereby denoting a characteristic instability of the outer films in the FRBs. Other subsynchronous motion with smaller amplitude locates at ~50% shaft speed, thus showing characteristics of the inner film instability. The subsynchronous frequencies of motion do not lock (whip) at system natural frequencies but continuously track with rotor speed. Most noticeably, the subsynchronous whirl motions of the ETC reach a limit cycle enabling continuous operation. The linear rotordynamic model predicts reasonably the onset speed of instability using linearized bearing force coefficients. However, the linear analysis cannot predict the severity of the subsynchronous whirl motions (i.e., its amplitude).

In real turbocharger operation, variations in oil supply conditions, rotor speed ramp rates, and mass imbalance configurations largely determine subsynchronous whirl frequency motions (amplitude and frequency) of the rotor-bearing system [16,33]. This is because, these motions are a result of the nonlinearity [34] and oil-whirl induced instability from hydrodynamic fluid film bearings (i.e., inner and/or outer films of FRBs) [26,28].

A prototype ETC is currently under construction. After the hardware is fabricated, the present rotor structural model will be tuned to match the measured free-free mode natural frequencies and mode shapes. Extensive imbalance response experiments will be performed to validate current predictions. More extensive thermal and mechanical analyses will continue to advance the current knowledge on the transient response of an ETC at a system level. Accurate and efficient computation tools, experimentally benchmarked, for prediction of turbocharger nonlinear rotordynamic response are essential to significantly reduce time in new turbocharger development with marked cost savings in product qualification. Future publication will continue to advance knowledge gained with this novel turbocharger technology.

ACKNOWLEDGMENTS

The work is conducted in a development partnership with Caterpillar (UK), Inc.

NOMENCLATURE

$\bar{C}$	Non-dimensional bearing damping coefficient
C	Global damping matrix
C_B	Bearing damping coefficient
c_r	Bearing radial clearance at room temperature
D	Rotor or floating ring diameter at room temperature
F	Vector of forces and moments
F_{Ext}	Vector of external excitation forces
F_{FRB}	Vector of bearing reaction forces
F_{Imb}	Vector of mass imbalance forces
F_S	Vector of static loads
G	Global gyroscopic matrix
$\bar{k}$	Non-dimensional stiffness coefficient
K	Global stiffness matrix
K_B	Bearing stiffness coefficient
L	Bearing film length at room temperature
M	Global mass matrix
u	Rotor instantaneous position
ζ	Damping ratio
μ	Lubricant viscosity
Ω	Shaft rotational speed

Acronyms

CW	Compressor wheel
ETC	Electric Turbocompound
FRB	Floating ring bearing
ICE	Internal combustion engine
ID	Inner diameter
OD	Outer diameter
RBS	Rotor-bearing system
SR	Switched reluctance
TW	Turbine wheel

REFERENCES

[1] Bernard, C., Rodica, B., 1999, *Diesel Engine Reference Book*, 2nd Edition, Society of Automotive Engineers, Inc, Warrendale, PA, Chapter 2.1.

[2] Mayer, M., 2001, *Turbochargers: Effective Use of Exhaust Gas Energy*, 2nd Edition, BorgWarner Turbo Systems, Verlag Moderne Industie, Landsberg/Lech, pp. 44.

[3] Petitjean, D., Bernardini, L, Middlemass, C., and Shahed, S. M., 2004, "Advanced Gasoline Engine Turbocharging Technology for Fuel Economy Improvements," SAE Paper No. 2004-01-0988

[4] Bumby, J.R., Spooner, E.S., Carter, J., Tennant, H., Mego, G.G., Dellora, G., Gstrein, W., Sutter, H., Wagner, J., 2004, "Electrical Machines for Use in Electrically Assisted Turbochargers," *Proceedings of the 2nd international conference on Power Electronics, Machines and Drives*, Edinburgh, UK, **1**, pp. 344-349.

[5] Ryder, O, Sutter, H., and Jaeger, L., 2006, "The Design and Testing of an Electrically Assisted Turbocharger for Heavy Duty Diesel Engines," *Proceedings of the 8th International Conference on turbochargers and Turbocharging*, CRC Press, Boca Raton, FL, pp. 157-166.

[6] Uchida, H., "Trend of Turbocharging Technologies," R&D Rev. Toyota CRDL, **41**(3), pp. 1-8.

[7] Fitzgerald, A. E., Kingsley, C. Jr., and Umans, S. D., 1991, *Electric Machinery*, 5th Edition, McGraw-Hill Publishing Company, New York, Chapter 10.

[8] Calverley, S.D., Jewell, G.W., Saunders, R.J., 1999, "Design of a High Speed Switched Reluctance Machine for Automotive Turbo-Generator Applications," SAE Paper No. 1999-01-2933.

[9] Hopmann, U., and Algrain, M. C., 2003, "Diesel Engine Electric Turbo Compound Technology," SAE Paper No. 2003-01-2294.
[10] Calverley, S.D., Jewell, G. W., and Saunders, R. J., 2005, "Prediction and Measurement of Core Losses in a High-Speed Switched-Reluctance Machine," IEEE Trans. Magnetics, **41**(11), pp. 4288-4298.
[11] Michon, M., Calverley S. D., Clark, R. E., Howe, D., McClelland, M., and Sykes, P., 2006, "Switched Reluctance Turbo-Generator for Exhaust Gas Energy Recovery," *Proceedings of the 12th International Power Electronics and Motion Control Conference*, Portoroz, Slovenia, pp. 1801-1807.
[12] Michon, M., Calverley, S.D., and Atallah, K., 2011, "Operating strategies for Switched Reluctance generators in exhaust gas energy recovery systems," *Proceedings of the 2011 IEEE International Electric Machines & Drives Conference*, Niagara Falls, ON, pp. 1609-1614.
[13] Trippett, R. J., and Li, D., 1983, "High-Speed Floating-Ring Bearing Test and Analysis," ASLE Trans., **27**(1), pp. 73-81
[14] Schweizer, B., 2009, "Total Instability of Turbocharger Rotors—Physical Explanation of the Dynamic Failure of Rotors with Full-Floating Ring Bearings," J. Sound Vibr., **328**(1-2), pp. 156-190.
[15] San Andrés, L., and Kerth, J., 2004, "Thermal Effects on the Performance of Floating Ring Bearings for Turbochargers," Proc. Inst. Mech. Eng., Part J: J. Eng. Tribol., **218**(5), pp. 437–450.
[16] Holt, C., San Andrés, L., Sahay, S., Tang, P., LaRue, G., and Gjika, K., 2005, "Test Response and Nonlinear Analysis of a Turbocharger Supported on Floating Ring Bearings," ASME J. Vibr. Acoust., **127**, pp. 107–212.
[17] San Andrés, L., Rivadeneira, J., Chinta, M., Gjika, K., and LaRue, G., 2007, "Nonlinear Rotordynamics of Automotive Turbochargers: Predictions and Comparisons to Test Data," ASME J. Eng. Gas Turbines Power, **129**(2), pp. 488–493.
[18] San Andrés, L., Rivadeneira, J. C., Gjika, K., Groves, C., and LaRue, G., 2007, "Rotordynamics of Small Turbochargers Supported on Floating Ring Bearings—Highlights in Bearing Analysis and Experimental Validation," ASME J. Tribol., **129**, pp. 391–397.
[19] San Andrés, L., Rivadeneira, J. C., Gjika, K., Groves, C., and LaRue, G., 2007, "A Virtual Tool for Prediction of Turbocharger Nonlinear Dynamic Response: Validation against Test Data," ASME J. Eng. Gas Turbines Power, **129**(4), pp. 1035–1046.
[20] San Andrés, L., Maruyama, A., Gjika, K., Xia, S., 2010, "Turbocharger Nonlinear Response with Engine-Induced Excitations: Predictions and Test Data," ASME J. Eng. Gas Turbines Power, **132**, p. 032502.
[21] Vance, J., Zeidan, F., and Murphy, B., 2010, *Machinery Vibration and Rotordynamics*, John Wiley & Sons, Inc., Hoboken, New Jersey, Chapter 4.
[22] American Petroleum Institute, 2010, *Rotordynamic Tutorial: Lateral Critical Speeds, Unbalance Response, Stability, Train Torsionals, and Rotor Balancing, API Recommended Practice 684*, 2nd Edition, Washington D.C., Sections 2 and 4.
[23] Mogenier, G., Dufour, R., Ferraris-Besso, G., Durantay, L, and Barras, N., 2010, "Identification of Lamination Stack Properties: Application to High-Speed Induction Motors," IEEE Trans. Indust. Electr., **57**(1), pp. 281-287.
[24] Chen, W. J., and Gunter, E. J., 2005, *Introduction to Dynamics of Rotor-Bearing Systems*, Eigen Technologies, Inc, Davidson, NC, Chapters 6 and 7.
[25] Timoshenko, S. P., and Goodier, J. N, 1970, *Theory of Elasticity*, McGraw-Hill, New York, pp. 80-83.
[26] Childs, D., 1993, *Turbomachinery Rotordynamics*, John Wiley & Sons, Inc., New York, Chapter 4.
[27] Soboyejo, W. O., 2003, Mechanical Properties of Engineered Materials, CRC Press, New York, Chapter 9.
[28] San Andrés, L., 2009, *Modern Lubrication Theory*, Class Notes 05. Dynamics of a Simple Rotor-Fluid Film Bearing system, Open source: http://repository.tamu.edu/handle/1969.1/93245, Accessed Nov. 2011.
[29] Ehrich, F., and Childs, D., 1984, "Self-Excited Vibrations in High Performance Turbomachinery," Mech. Eng., **106**(5), pp. 66–79.
[30] Noah, S., and Sundararajan, P., 1995, "Significance of Considering Nonlinear Effects in Predicting the Dynamic Behavior of Rotating Machinery," J. Vib. Control, **1**, pp. 431-458
[31] Nayfeh, A. H., and Balachandran, B., 1989, "Modal Interactions in Dynamical and Structural Systems," ASME Appl. Mech. Rev., **42**, pp. 175-201
[32] Kirk, R. G., Alsaeed, A. A., and Gunter, E. J., 2007, "Stability Analysis of a High-Speed Automotive Turbocharger," STLE Tribol. Trans., **50**, pp. 427-434.
[33] San Andrés, L., and Vistamehr, A., 2010, "Nonlinear Rotordynamics of Vehicle Turbochargers: Parameters Affecting Sub Harmonic Whirl Frequencies And Their Jump," *Proceeding of the 8th IFToMM International Conference on Rotor Dynamics*, Seoul, Korea, Sep. 12-15, Paper No. WeE3-2.
[34] Yamamoto, T., and Ishida, Y., 2001, *Linear and Nonlinear Rotordynamics: A Modern Treatment with Applications*, John Wiley & Sons, Inc., New York.